RESEARCH PAPER

CrossMark

Soft lithography fabrication of index-matched microfluidic devices for reducing artifacts in fluorescence and quantitative phase imaging

Diane N. H. Kim[1] · Kevin T. Kim[2] · Carolyn Kim[1] · Michael A. Teitell[1,3] · Thomas A. Zangle[4]

Abstract
Microfluidic devices are widely used for biomedical applications based on microscopy or other optical detection methods. However, the materials commonly used for microfabrication typically have a high refractive index relative to water, which can create artifacts at device edges and limit applicability to applications requiring high-precision imaging or morphological feature detection. Here we present a soft lithography method to fabricate microfluidic devices out of MY133-V2000, a UV-curable, fluorinated polymer with low refractive index that is close to that of water ($n = 1.33$). The primary challenge in the use of this material (and fluorinated materials in general) is the low adhesion of the fluorinated material; we present several alternative fabrication methods we have tested to improve inter-layer adhesion. The close match between the refractive index of this material and aqueous solutions commonly used in biomedical applications enables fluorescence imaging at microchannel or other microfabricated edges without distortion. The close match in refractive index also enables quantitative phase microscopy imaging across the full width of microchannels without error-inducing artifacts for measurement of cell biomass. Overall, our results demonstrate the utility of low-refractive index microfluidics for biological applications requiring high-precision optical imaging.

Keywords Microfluidic device · Microfabrication · Refractive index · Fluorescence imaging · Quantitative phase imaging

1 Introduction

Microfluidic devices have shown tremendous utility for studying biological samples (Sackmann et al. 2014). The small scale of microfluidic systems allows users to match the device length scale to the size of cells or even biological macromolecules, enabling precise control over the cellular environment (Weibel et al. 2007; Whitesides 2006; Zare and Kim 2010), massively parallel sample processing (Thorsen

✉ Thomas A. Zangle
  tzangle@chemeng.utah.edu

[1] Department of Bioengineering, University of California, Los Angeles (UCLA), Los Angeles, CA, USA

[2] Department of Neuroscience, UCLA, Los Angeles, CA, USA

[3] Department of Pathology and Laboratory Medicine, David Geffen School of Medicine, Broad Stem Cell Research Center, California Nanosystems Institute, and Molecular Biology Institute, UCLA, Los Angeles, CA, USA

[4] Department of Chemical Engineering and Huntsman Cancer Institute, University of Utah, Salt Lake City, UT, USA

et al. 2002), and high-sensitivity detection of biologically relevant parameters (Chung et al. 2011a; Yeo et al. 2011).

The utility of microfluidic devices is largely determined by the mechanical, chemical, and optical properties of the material used for fabrication. Accordingly, many different materials have been explored for different applications (Table 1). These materials include plastics, such as polystyrene and polymethylmethacrylate (PMMA) (Heckele and Schomburg 2004; Yeh et al. 2009); biologically derived materials, such as collagen gels and gelatin (Golden and Tien 2007; Paguirigan and Beebe 2006; Vickerman et al. 2008); and UV-curable polymers (Bartolo et al. 2008; Yan et al. 2017). Of the various available fabrication materials, polydimethylsiloxane (PDMS) is the most widely used for biological applications, for its ease of fabrication via soft lithography and biocompatible properties (McDonald and Whitesides 2002; Sackmann et al. 2014; Xia and Whitesides 1998). However, while certain material properties such as Young's modulus (Quake and Scherer 2000), biocompatibility, electrochemical properties (Kirby and Hasselbrink 2004), and surface tension (Lam et al. 2002) of various common microfabrication

Table 1 Summary of properties of selected common microfluidic materials

Material name	Type	Refractive index	Elastic modulus	Fabrication method	References
Polystyrene	Thermoplastic polymer	1.60	3–3.5 GPa	Injection molding	Zare and Kim (2010)
Polycarbonate	Thermoplastic polymer	1.58	2–2.4 GPa	Hot embossing	Wabuyele et al. (2001)
NOA 81	Adhesive polymer	1.56	200 kPa	Soft lithography (UV cure)	Bartolo et al. (2008) and Yan et al. (2017)
Glass	Glass	1.52–2.42	50–90 GPa	Etching	Choi et al. (2002)
Cyclic olefin polymer	Thermoplastic polymer	1.51–1.59	45–78 MPa	Injection molding	Nunes et al. (2010)
Polymethylmethacrylate (PMMA)	Thermoplastic polymer	1.50	1.8–3.1 GPa	Injection molding	Heckele and Schomburg (2004) and Yeh et al. (2009)
Polyurethane (PU)	Thermoplastic polymer	1.50	55 MPa	Solvent casting	Huang et al. (2016) and Pérez-Madrigal et al. (2014)
Polyethylene glycol diacrylate (PEGDA)	Elastomer	1.47	~ 1.6 MPa	Soft lithography (cross-linking)	Chung et al. (2012), Huang et al. (2016) and Mazzoccoli et al. (2010)
Fused silica	Glass	1.46	71.7 GPa	Etching	Dave et al. (2008) and Zangle et al. (2009)
Polydimethylsiloxane (PDMS)	Elastomer	1.41	360–870 kPa	Soft lithography (heat cure)	Xia and Whitesides (1998)
Collagen	Extracellular matrix	1.36–1.42	0.5–12 kPa	Injection molding (cross-linking)	Leonard and Meek (1997)
MY133-V2000	Adhesive polymer	1.334	4.5 MPa	Soft lithography (UV cure)	Kim et al. (this work)
MY133	Adhesive polymer	1.332	4 MPa	Soft lithography (UV cure)	Kim et al. (this work)
Water	–	1.331	–	–	–

materials have been extensively studied, optical properties other than transparency have not typically been considered. For example, the high refractive index of PDMS relative to water ($n_{PDMS} \sim 1.41$; $n_{water} \sim 1.33$) makes it prone to imaging artifacts at channel edges due to refraction and scattering.

Many common microfluidic applications employ optical detection or analysis methods (Andersson and van den Berg 2003), making optical properties and impact on measurement precision important factors that need to be considered when choosing materials. For example, fluorescence labeling enables the positive identification of cells and different cellular components with a high degree of specificity and has been used within microfluidic systems in a large variety of applications (Baret et al. 2009; Dittrich and Manz 2006; Jovic et al. 2009; Sackmann et al. 2014; Wang et al. 2005). The use of PDMS or other high-refractive index materials in microfluidic applications where the subject being imaged is close to microfabricated structures, either edges of microwells or other structures designed to control the positioning of the sample, can induce artifacts that compromise the integrity of the measurements. This is especially relevant in applications to live cell imaging where cells are often located in corners, or microfabricated cell traps may be used

to precisely position single cells for high-throughput analysis (Di Carlo et al. 2006).

The high difference in refractive index between aqueous media and microchannel materials also hinders the application of microfluidics to monitoring biological processes with quantitative phase microscopy (QPM) (Chun et al. 2012; Mir et al. 2011; Zangle et al. 2013a). QPM measures the phase shift of light as it passes through and interacts with matter inside of a transparent sample (Zangle and Teitell 2014). In measurements of single or clustered cells, QPM phase shift measurements can be used to measure cell mass over time using the known relationship between refractive index and biomass density, which is then used to compute cell mass (Zangle and Teitell 2014). Phase shift measurements with many QPM techniques contain inherent ambiguities due to the fact that light waves at two locations in the image can appear the same when they are perfectly in or out of phase by an integer multiple of one wavelength (Ghiglia and Pritt 1998; Kim et al. 2015). This ambiguity is typically resolved by a process known as phase unwrapping (Ghiglia and Pritt 1998). However, phase unwrapping is prone to errors at sharp changes in the optical path length of transmitted light through the sample, as occurs at the edges of high-refractive index microchannels filled with aqueous solutions. These phase-unwrapping errors reduce the

accuracy of mass measurements using QPM and prevent high-throughput measurements using most interferometric QPM methods (Jang et al. 2010; Lue and Popescu 2006).

The benefits of matching the refractive index of material and media are well known and have been used, for example, to study fluid behavior (Budwig 1994; Byron and Variano 2013), or to image intact whole organisms (Chung et al. 2013). However, common approaches to matching refractive index require either the use of porous hydrogels or increasing the refractive index of the media itself (Budwig 1994; Byron and Variano 2013). Both of these approaches may be problematic for use in a microfluidic system for biological applications, because of mixing of defined media conditions in adjacent chip locations (Sun et al. 2017) or because cells may not tolerate changes in media conditions sufficient to match refractive index. Fluorination can be used to reduce the refractive index of organic polymers based on the low polarizability of fluorine (Groh and Zimmermann 1991); however, the resulting materials are Teflon-like with reduced inter-layer adhesion.

In this paper, we present a protocol for fabricating low-refractive index ($n = 1.33$) fluoropolymer microfluidic devices, which drastically reduce the occurrence of image artifacts at the edges of channels filled with aqueous solutions. This protocol is based on the MY133 series of UV-curable low-refractive index polymers with refractive index very close to that of water ($n_{MY133} \sim 1.33$), which are primarily used as optical adhesive or coating material. The low refractive index and high-fidelity feature reproduction of MY133 mean that this material can potentially be used for a wide range of applications requiring high-precision optical measurements, including fluorescence and quantitative phase imaging. Therefore, we established a protocol to utilize MY133 as a material for microfabrication based on soft lithography for high-quality feature reproduction and additional processing to promote inter-layer adhesion and make the material biocompatible for biomicrofluidic applications. We demonstrate multiple advantages of using MY133 polymer for high-precision optical imaging, such as reduced fluorescence artifacts at channel and structure edges. In addition, we show that QPM mass measurements of cells can be taken in these channels reproducibly. We therefore demonstrate that MY133 polymer is an ideal fabrication material for both high-precision fluorescence and QPM imaging in biological or other aqueous applications.

2 Methods and materials

2.1 Preparation of molds and materials

100-µm-high photoresist (SU-8 3050, Microchem) molds on silicon wafers were fabricated using contact alignment, chrome-mask photolithography (Karl Suss MA6 Contact Aligner). All molds for fabrication (SU-8 or PDMS) were treated with fluorosilane (trichloro(1H, 1H, 2H, 2H-perfluorooctyl)silane, Sigma-Aldrich) in a vacuum chamber prior to use.

Glass slides (Fisher's finest glass slides) or ibidi μ-dishes with standard bottom, a gas-permeable cell culture substrate, were exposed to air plasma (Harrick Plasma PDC-32G) for 60 s before undergoing methacrylate (3-(trimethoxysilyl) propyl methacrylate, 98%, Sigma-Aldrich) coating in a vacuum chamber for 4 h. After methacrylate treatment, slides were dried in an oven for 1 h before being stored for use.

2.2 MY133 device fabrication

MY133 devices were fabricated via soft lithography, as shown in Fig. 1. To create the layer containing the channel, MY133-V2000 (Electro Optical Components and MY Polymers) (henceforth "MY133") was deposited on the surface of a patterned PDMS mold inside of a PDMS boundary to define device edges. After 15 min under vacuum to get rid of air bubbles in the polymer, a single quartz glass slide was laid on top, enclosing the MY133 between PDMS, the boundary, and the quartz (Fig. 1a). This was then cured under ultraviolet (UV) illumination using a UV cure oven (IntelliRay Uvitron UV Flood Curing System). This resulted in a cured MY133 layer with a thin layer of uncured polymer due to oxygen inhibition of cross-linking (Fig. 1a). We did not note any difficulty in removing the cured MY133 device from fluorosilane-treated PDMS molds. The same process was repeated with a flat PDMS layer to create the bottom layer of the MY133 microdevice (Fig. 1b). Afterward, the uncured sides of both layers were brought in contact while taking care not to disturb the uncured layers, and cured under UV in deionized (DI) water on top of the substrate, creating a permanently bonded device (Fig. 1c).

We also tested other variations on this basic fabrication protocol. One simplified method is to fully cure MY133 channel on the SU-8 master wafer or PDMS mold. Then, both the MY133 construct (channel side up) and substrate are plasma-treated (Harrick Plasma PDC-32G) before attachment. This results in an impermanent bond between the construct and slide, but with significantly reduced complexity.

To create microwell devices, MY133 was placed directly onto methacrylate-treated glass or silicon slides. Then a PDMS microwell mold was pressed onto the slide and the construct immersed in DI water to prevent oxygen from inhibiting the curing reaction. This assembly was then cured by UV exposure for 60 s before removal of the PDMS mold and final curing under DI water for 60 s. Finally, the device was rinsed thoroughly in ethanol to remove uncured monomer.
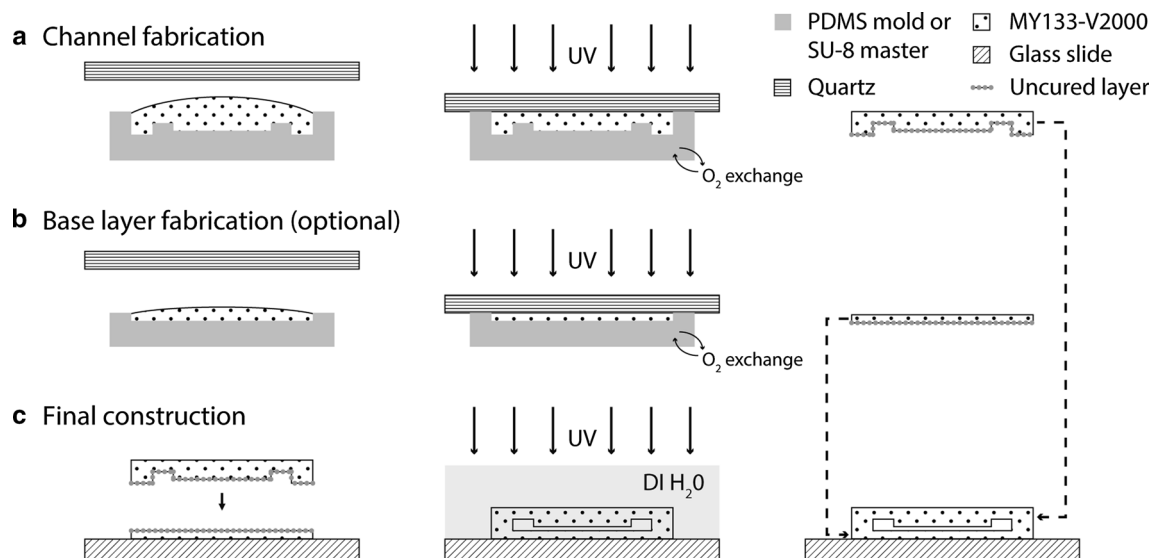
a Channel fabrication

b Base layer fabrication (optional)

c Final construction

Fig. 1 Overview of MY133 soft lithography process flow. **a** PDMS molds are made by soft lithography from SU-8 on silicon and used to fabricate MY133-V2000 channels via UV-curing through a quartz top layer. Efficient gas exchange through PDMS mold allows for O_2 to inhibit polymerization at the device surface, leaving a thin uncured layer. **b** Optionally, a uniform-thickness MY133-V2000 base layer may be used to improve adhesion. **c** A final cure in deionized (DI) H_2O completes the polymerization reaction

2.3 PDMS device fabrication

PDMS channels were cast from SU-8 molds following standard approaches (McDonald and Whitesides 2002). Briefly, PDMS mixed at 10:1 base:curing agent ratio was poured onto the mold, vacuum-treated to reduce air bubbles, and fully cured (Thermo Fisher Scientific). After curing, inlets and outlets were created using a 0.75-mm punch, and then both PDMS channels and glass slides were exposed to air plasma (Harrick Plasma PDC-32G) for 60 s and attached to form a permanent bond.

2.4 Imaging

Microscopy was performed on a Zeiss Axio Observer A1 with stage-top incubation system (Zeiss). Fluorescence, brightfield, and QWLSI quantitative phase imaging were performed using either a 10×0.25 numerical aperture (NA), 20×0.4 NA, or 40×0.5 NA objective. Phase contrast imaging was performed using a 20×0.4 NA Ph2 objective. Fluorescence, brightfield, and phase contrast images were captured with a Hamamatsu EM-CCD Digital Camera C9100 camera. QPM data were captured with a SID4Bio quadriwave lateral shearing interferometry (Phasics) camera (Bon et al. 2009). A 0.35 NA condenser was used for transillumination with a halogen lamp for phase contrast, a 660-nm collimated LED (Thorlabs) for QPM, and a X-Cite Series 120 Q fluorescence light source for fluorescence imaging.

2.5 Fluorescence image analysis

Fluorescence microscopy images were analyzed using MATLAB (the Mathworks). Briefly, a threshold of 0.7 of maximum intensity was applied to generate a binary image of the fluorescent beads. A MATLAB built-in function for eccentricity measurement was then used on each shape in the binary image to quantify the eccentricity of bead images by computing the ratio of the length of the ellipse major axis to the distance between foci. (The limit of 0 corresponds to a circle and 1 is a straight line.)

2.6 Optical profilometry

Optical profilometry was performed using a Bruker Contour GT-X8 (Bruker) in high-resolution vertical scanning interferometry (VXI) mode. Refractive index was determined by first measuring channel step height in air, then filling the channels in water, and measuring the step height change in optical path difference between the channel and the surrounding material using a 20×, 0.28 NA through transmissive media (TTM) objective. Shrinkage during curing was determined using the affine transformation matrix returned by MATLAB's imregister function (500 iterations) comparing the inverted MY133 channel profilometry data to profilometry data from the SU-8 master mold. QPM data of water-filled microchannels with the Bruker system were acquired as described and validated previously (Chun et al. 2012; Reed et al. 2011; Zangle et al. 2013b) for live cell imaging in phase shifting interferometry (PSI) mode.

2.7 Cell culture

MY133 channels constructed on top of gas-permeable polymer coverslips (ibidi 35-mm cell culture dishes, cat # 81156) were rinsed with sterile filtered 100% ethanol for 2 h, followed by a 24-h rinse with sterile deionized (DI) water. Channels were coated by filling with 10 μM fibronectin (Sigma-Aldrich) in DI water and allowed to dry for 1–3 h at room temperature. The channel was then rinsed with DPBS before seeding M202 cells (Søndergaard et al. 2010) at a concentration of approximately 10^6 cells/mL. After 30 min of incubation, the channel was rinsed with cell medium before connecting to a perfusion unit.

M202 cells were cultured as described previously (Søndergaard et al. 2010). The cell medium was composed of RPMI 1640 (Fisher), 10% fetal bovine serum (Omega), and 1% penicillin–Streptomycin solution (Corning) buffered with 20 mM HEPES (Thermo Fisher Scientific), under continuous perfusion using a syringe pump (Harvard Apparatus Pump 11 Elite).

M202 cells were seeded in 12-well plates (Corning) at a concentration of 10^4 cells per well in 1 mL of cell media. One plate was used as control; each well on the other plate had a piece of cured and treated MY133 polymer submerged in cell culture media. After 12 h for cell attachment, each well of M202 cells was detached and counted manually using a hemacytometer. The cells were counted for 5 days in triplicate per day per condition.

2.8 QPM data analysis

QPM data analysis was performed using custom MATLAB scripts as previously described (Reed et al. 2011). Briefly, cells were segmented from the background using a combination of local thresholding and edge detection. Cells mass was then computed from QPM data using an assumed cell average-specific refractive increment of 1.8×10^{-4} m^3/kg (Zangle and Teitell 2014). Mass versus time tracks were compiled by using an algorithm that links cell data from frame to frame by minimizing the displacement of each identified cell in terms of *x* location, *y* location, and mass (Crocker and Grier 1996).

3 Results and discussion

3.1 Resolution of feature reproduction in MY133 via soft lithography

To evaluate the fabrication resolution of the MY133, we used optical profilometry to measure the features on the original SU-8 master and resultant MY133 device created using the same device mold. Profiles of the mold and the device showed precise reproducibility of the master mold by MY133 (Fig. 2a–c) with less than 1% shrinkage during curing, which compares well to the estimated 1.2% shrinkage during curing estimated by the MY133 manufacturer. In addition, we also found that MY133 also features slightly reduced surface roughness relative to that of PDMS (Fig. 2d).

3.2 Refractive index of MY133 and PDMS devices

MY133 polymer is fluorinated in order to reduce the polarizability of the material and, therefore, the refractive index (Groh and Zimmermann 1991). The resulting refractive index of MY133 closely matches that of water, which confers several advantages in applications requiring fluorescence and quantitative phase imaging. In air, both PDMS and MY133 devices are clearly visible due to high difference in refractive index ($n_{air} \sim 1.00$; $n_{water} \sim 1.33$) (Fig. 3a, c). However, when placed under water, the perimeter of PDMS device is clearly visible (Fig. 3b) and the edges of MY133 device of same pattern and dimensions become invisible except for the air trapped in the channel portion (Fig. 3d). The difference in refractive index is also clearly visible in phase contrast images of water-filled channels (Fig. 3e, f). In these images, PDMS has high-intensity pixels at the channel edges due to the large difference in refractive index between the channel material and the water filling the channel, while MY133 does not (Fig. 3g). To verify refractive index, we also calculated refractive index of both polymers (Fig. 3h) using optical
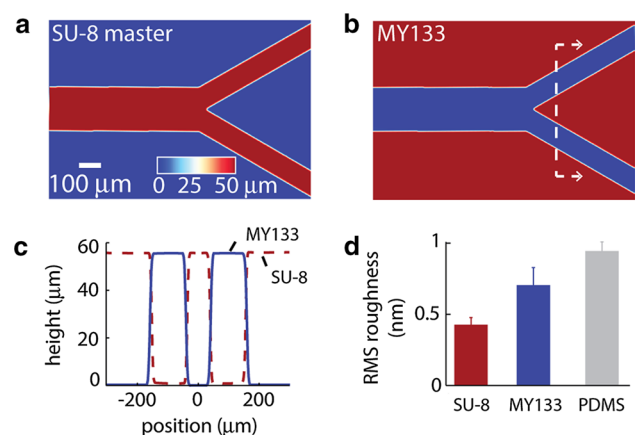

Fig. 2 MY133 shows excellent feature reproduction in microfabricated devices. **a** Optical profilometer image of SU-8 master mold and **b** MY133 soft lithography result. Dashed line shows location of cutout in panel (**c**). **c** Optical profilometry cross section comparing MY133 device to original SU-8 master mold shows minimal shrinkage (< 1%) during MY133 device curing. **d** MY133 shows moderately reduced surface roughness relative to PDMS and comparable roughness to the SU-8 master used for fabrication. Error bars show standard deviation
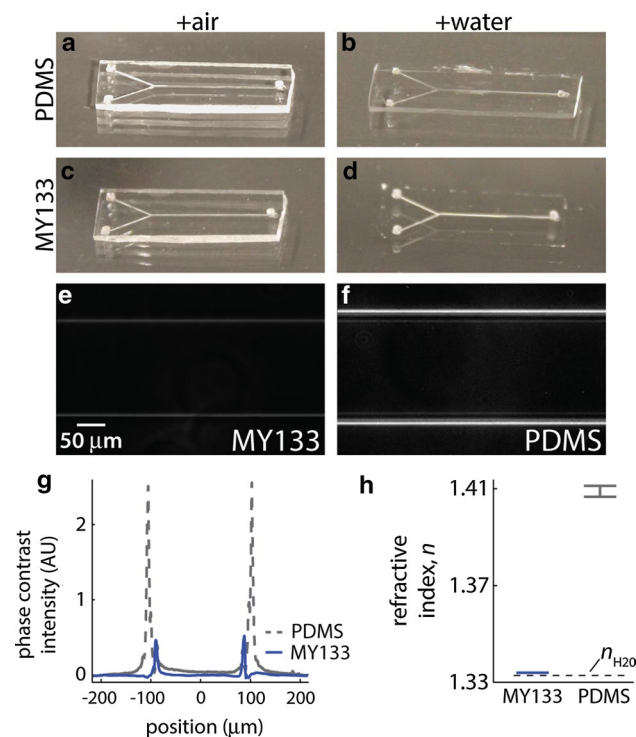
Fig. 3 MY133 has a refractive index close to that of water. Photograph of MY133 (bottom) and PDMS (top) air-filled 100-μm-deep microchannel devices in (**a**, **c**) air and (**b**, **d**) water shows the close match in refractive index as a near-elimination of MY133 device edges when immersed in water. **e** Phase contrast image of 100-μm-deep, water-filled MY133 microchannel taken in same conditions (exposure time and illumination and optics) as **f** phase contrast image of PDMS channel. **g** MY133 channel shows much lower contrast at channel edges in channel intensity profiles averaged along the length of the channel. **h** Refractive index of MY133 devices at 660 nm is closely matched to water ($\Delta n_{H2O} < 1 \times 10^{-3}$). Error bars show standard deviation

profilometry, which closely followed that of the reported values for MY133 and PDMS (Xia and Whitesides 1998).

Our measured refractive index at 660 nm is comparable to manufacturer data specifying a refractive index for cured MY133-V2000 of 1.333 and 1.329 at 589 and 950 nm, respectively. The refractive index of water ranges from approximately 1.332 to 1.327 for the same wavelength range. Therefore, the difference in refractive index of this material relative to water is small across a range of wavelengths. Additionally, MY133-V2000 only exhibits a small change in refractive index during curing (from 1.330 to 1.333); therefore, curing conditions do not play a major role in determining final device properties. Throughout our experiments, the refractive index was generally consistent at both room temperature and 37 °C (cell culture conditions), so we do not expect the refractive index to vary in normal conditions (e.g., non-extreme temperatures).
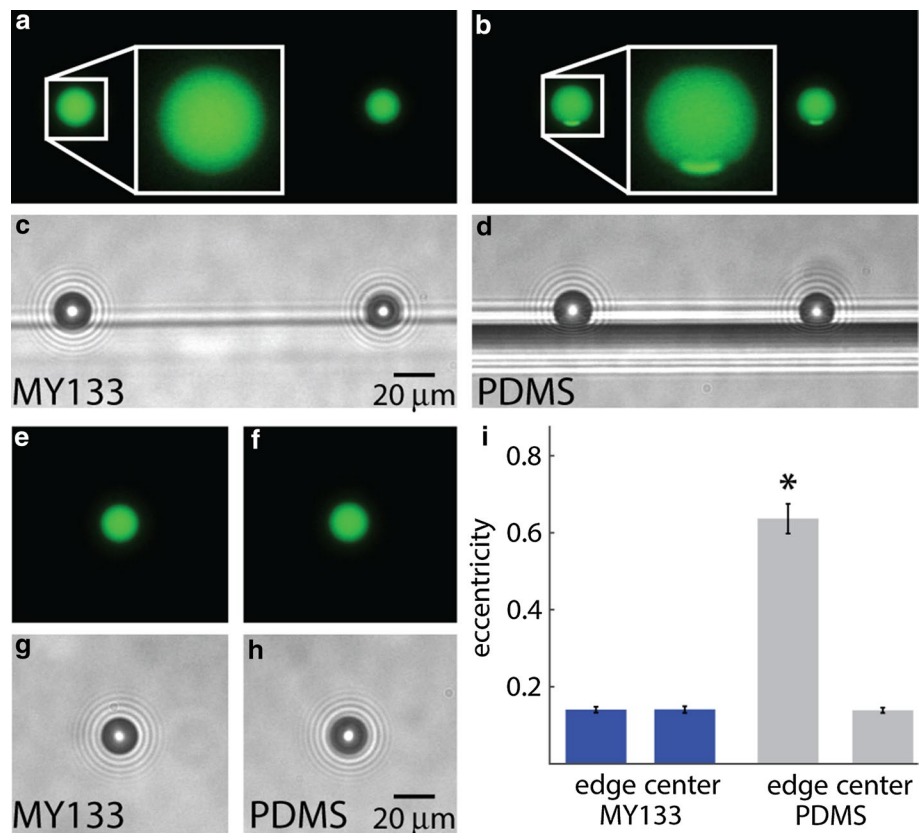
3.3 Elimination of artifacts at microfabricated structures in fluorescence imaging

The low refractive index of MY133 is advantageous for fluorescence imaging. Often, the intensity and the area of features in fluorescence images are measured to draw quantitative conclusions about the role of the labeled object or structure (Giepmans et al. 2006; Ntziachristos 2006). Microfluidic systems are often used in conjunction with fluorescent imaging to control and manipulate the specimen being measured and its environment. However, the material used to fabricate the microfluidic device can have an impact on the accuracy of features quantified with fluorescence microscopy. In order to quantify this effect, we imaged spherical, green fluorescent beads as a model system with known geometry in the middle and at the edge of straight microfluidic channels (Fig. 3) using widefield fluorescence microscopy. When the beads were positioned at the edge of the channel in an MY133 device, fluorescence images remained comparable to beads at the center of the device, maintaining their expected spherical shape (Fig. 4a, c). In contrast, beads positioned at PDMS channel edges showed artifacts where the bead touched the channel wall (Fig. 4b, d). This can be attributed to the high difference between refractive index of water and of PDMS, as beads in the center of MY133 PDMS channels also show undistorted fluorescence (Fig. 4e–h). In order to quantify the effects of artifact at PDMS channel edges, we calculated eccentricity as a measure of departure from the expected circular shape. Image segmentation based on fluorescence images was used to outline the edge of the fluorescence shape. Eccentricity (*e*) of each individual bead was then calculated based on the fluorescence images as the ratio of the major axis to the distance between foci of an ellipse with the same second moments as the region. For a perfect circle, the eccentricity is zero, and as ellipses deviate from a circle, the eccentricity nears a value of 1. As shown in Fig. 4i, the eccentricity of fluorescent beads was significantly higher than beads in three other conditions, showing that fluorescent images at PDMS channel edges result in artifacts that can compromise the integrity of the fluorescence measurements.

3.4 Elimination of artifacts at microfabricated structures in quantitative phase imaging

Next, we tested the applicability of MY133 in QPM in order to study whether or not MY133 would be an ideal material to integrate microfluidics with QPM. QPM is highly applicable in biological studies as it enables precise measurements of dry masses of biological samples by measuring the phase shift of light as it passes through a sample (Popescu et al. 2014; Zangle and Teitell 2014). These measurements of dry biomass in cells over time have many practical applications,

Fig. 4 MY133 devices reduce artifacts in fluorescence imaging. **a–d** 16-μm spherical fluorescent polystyrene beads at the edge of channel structures in MY133 and PDMS microchannels. **a**, **b** Fluorescence and **c**, **d** brightfield images show artifacts in PDMS channels. Beads imaged at the edge of MY133 channels **a**, **c** show results comparable to (**e–h**) fluorescent and brightfield images at the center of microchannels. **i** Eccentricity measurements of fluorescent bead images show significant aberrations in images of beads at PDMS channel edges. Lower eccentricity indicates a more rounded shape, as expected for images of spherical beads. *$p < 0.01$, $n = 38, 28, 30, 30$ for MY133 edge, MY133 center, PDMS edge, and PDMS center, respectively; error bars show standard error of the mean

such as rapid drug screening, study of interaction between different cell types, and study of specific inter-cellular structures (Kandel et al. 2017; Reed et al. 2011; Zangle et al. 2013a).

Direct phase shift measurements taken with QPM typically must be processed by a phase-unwrapping algorithm to yield an image of the true phase shift due to inherent phase ambiguities (Ghiglia and Pritt 1998; Goldstein et al. 1988). However, these methods are susceptible to phase-unwrapping errors when local differences in optical path length within the sample exceed 2π rad or one wavelength of the light source used for illumination. The result is reduced measurement accuracy and precision (Kim et al. 2015). A rule of thumb to avoid phase-unwrapping errors in QPM is to ensure that:

$$OPD_{max} < \lambda, \tag{1}$$

where OPD_{max} is the maximum difference in optical path length between adjacent pixels within the image and λ is the wavelength of light used for sample illumination. OPD can be computed as:

$$OPD = \overline{\Delta n} \cdot h, \tag{2}$$

where $\overline{\Delta n}$ is the average difference in refractive index between adjacent locations of the sample, through h, the thickness of the sample. At channel or microstructure edges,

the OPD is therefore the difference in refractive index of the material relative to water times the channel height. This places a practical limit on the maximum practical microchannel height for use with QPM, based on refractive index. For example, for a 100-μm-deep channel illuminated with green light at $\lambda = 500$ nm, $\Delta n_{max} = 5 \times 10^{-3}$.

MY133 devices have a refractive index difference relative to water that keeps the optical path difference below this practical limit on quantitative phase imaging, $\Delta n < 1 \times 10^{-3}$ (Fig. 3f). To demonstrate the applicability of MY133 microfluidic devices, we imaged both MY133 and PDMS microchannels filled with water with each of two different interferometric QPM methods (Fig. 5), using two different height (approximately 100 and 50 μm) channels. In quadriwave lateral shearing interferometry (QWLSI), an interferogram is used to compute the gradient of phase shift which is then numerically integrated to yield phase shift (Bon et al. 2012). In phase shifting interferometry (PSI), an interferogram is used to directly compute the phase shift (Reed et al. 2011; Schmit et al. 1993). In each case, QPM images of PDMS channels showed pronounced artifacts originating from microchannel boundaries (Fig. 5b, d). These errors can significantly reduce QPM measurement accuracy, as reflected in the high ranges of phase shift intensities of the two measurements in QWLSI and PSI (700 and 6000 nm, respectively). However, these errors are eliminated in QPM
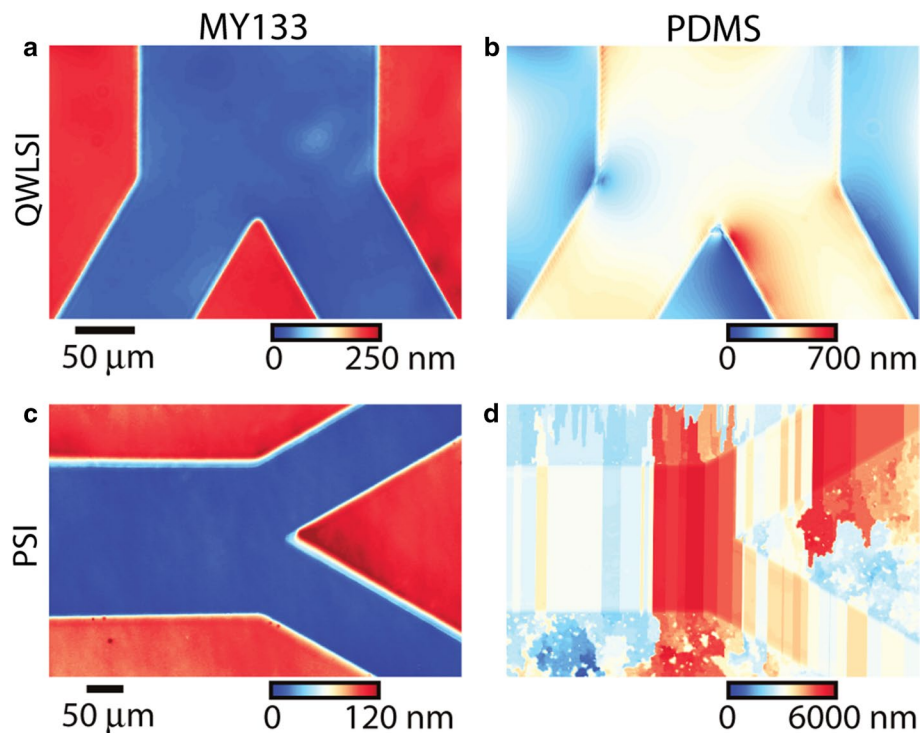
Fig. 5 MY133 microfluidic devices are effective for QPM imaging. **a** QPM image via quadriwave lateral shearing interferometry (QWLSI) of water-filled MY133 ($h = 100$ μm) device shows no artifacts at channel edges. **b** QPM images of water-filled PDMS channels ($h = 100$ μm) taken with the same technique as in (**a**) show variable, localized errors due to phase unwrapping. These errors are larger than the entire measured phase shift in the MY133 device. (Note the difference in scale used for phase colormap.) **c** QPM image of water-filled MY133 channel ($h = 50$ μm) taken with phase shifting interferometry (PSI). **d** QPM image of water-filled PDMS channel ($h = 50$ μm) taken with PSI shows large phase-unwrapping errors propagating across the channel structure. The magnitude of the resulting QPM images (note scale bar difference from **c** to **d**) far exceeds the measured phase shifts in this image, indicating that it would be difficult or impossible to make meaningful QPM measurements within the PDMS channel

measurements of microchannels fabricated with MY133 (Fig. 5a, c). In measurements of MY133 devices, QWLSI data using 100-μm channel show double the phase shift inside versus outside the channel as for PSI using 50-μm channel, as expected. As in fluorescence imaging, the low refractive index of MY133 enables more accurate QPM measurements.

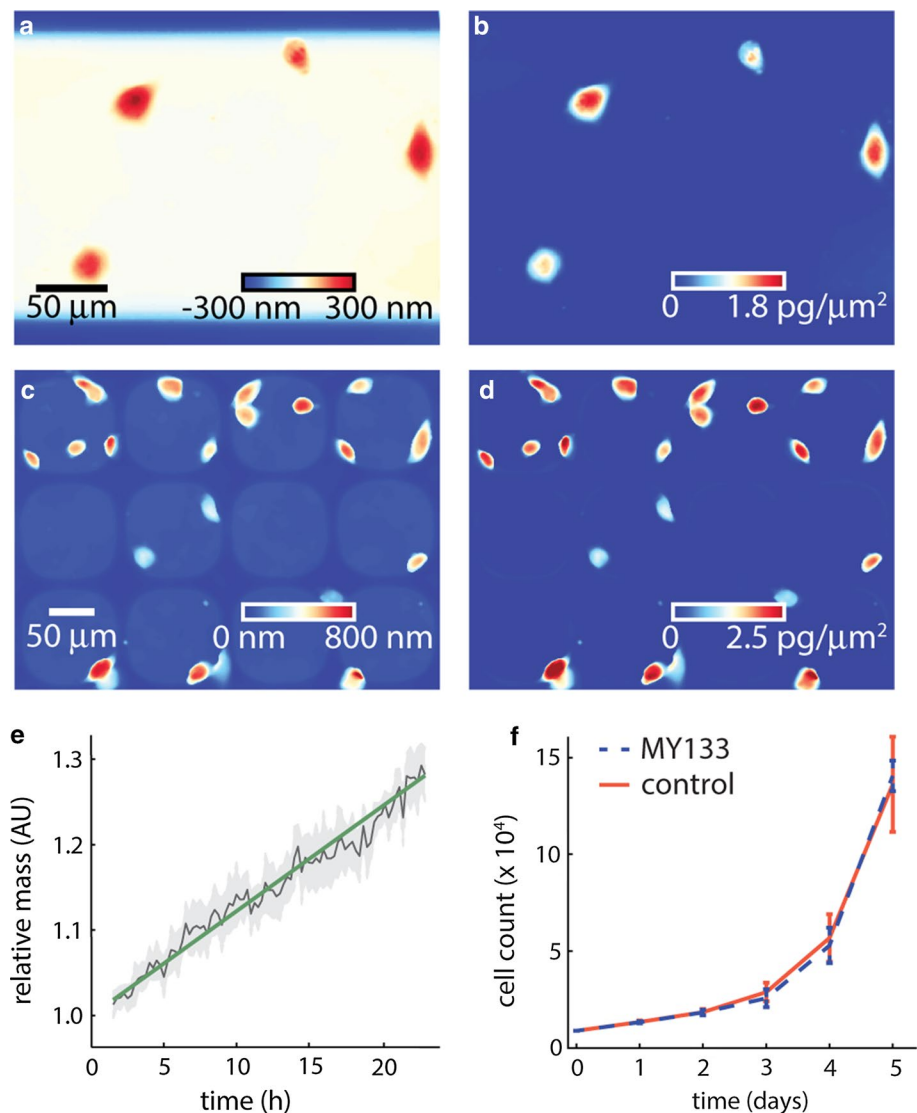### 3.5 MY133 enables measurement of cell biomass accumulation rate over time via quantitative phase imaging

MY133-fabricated microstructures are suitable for cell culture, enabling high-precision optical imaging for biomedical applications. As a demonstration, we fabricated MY133-V2000 microchannels (Fig. 6a, b) and MY133 microwells (Fig. 6c, d) and prepared them for cell culture. We determined it was necessary to rinse MY133 structures with 100% ethanol (EtOH) followed by sterile DI water to prevent cytotoxicity due to uncured MY133 monomer. Devices were then coated in fibronectin to promote cell attachment.

The low refractive index of MY133 enables error-free QPM measurements of cells within both closed microchannels and open microwell structures (Fig. 6a, c). In QPM images, these structures can be masked out via image processing (Fig. 6b, d) to yield images of the mass distribution within cells (Zangle and Teitell 2014). Measurements of cell mass from QPM data confirmed that cells grow and accumulate mass when cultured in MY133 channels (Fig. 6e). Cells grown in cell culture wells containing cured MY133 or in control conditions (standard cell culture wells in the absence of MY133) showed the same overall population doubling time, confirming that MY133 material is appropriate for cell culture (Fig. 6f). This demonstrates the applicability of MY133 for future use in biological studies.

4 Conclusions

We have demonstrated the novel use of a low-refractive index fluoropolymer, MY133, in fabricating microfluidic channels via a soft lithography process. The fluorination of this material is necessary to lower the material's refractive

Fig. 6 MY133 microfluidic devices for quantitative phase imaging of live cells. **a** QPM image (via QWLSI) of M202 cells in a 100-μm-high MY133-V2000 microchannel shows uniform background. **b** QPM image from (**a**) with channel masked out allows for quantification of cell biomass distributions. **c** QPM image of M202 cells in 12-μm-high MY133 microwells showing artifact-free images of cells in close contact with microfabricated structures. **d** QPM image with microwells removed via image processing (by subtracting the average phase profile of microwells from multiple frames) showing the distribution of cell biomass in microwell structures. **e** Measurements of cell mass over time, normalized by cell initial mass to account for variations in cell size, for cells imaged within MY133 channels. These data demonstrate the robust growth within MY133 devices ($n = 21$). Mean mass is shown in blue, linear fit in green, and ± standard error of the mean in gray. **f** Cell proliferation when exposed to MY133 shows the same overall proliferation rate as control cells cultured in the absence of MY133. Error bars show standard error of the mean

index (Groh and Zimmermann 1991), but at the cost of reduced inter-layer adhesion. We have therefore developed several strategies to fabricate microstructures that are compatible with the constraints of cell growth. We have also shown that the low refractive index of MY133 confers advantages in fluorescent and quantitative phase imaging relative to high-refractive index materials. Finally, we demonstrated the applicability of MY133-microfabricated devices to cell culture in closed microchannel and open microwell structures.

There are several additional practical considerations regarding the use of MY133. We found that this material has low gas permeability once cured; therefore, for prolonged cell culture a gas-permeable substrate can be used to maintain O_2 and CO_2 levels in cell media. The adhesion between same polymer constructs is permanent as long as the integrity of uncured layer is maintained at the time of adhesion formation. Adhesion to glass or other substrates

using the methods outlined in this paper can be maintained at cell culture conditions (high humidity and warm temperature) for up to 24 h without leaking, sufficient to perform a typical imaging assay. If used without the high humidity and temperature required for cell culture the adhesion lasts longer. Adhesion for long-term cell culture (> 24 h) could be improved, for example, via mechanical clamping of the MY133 devices. Creation of vias and connections to tubing in MY133 is very easy and can be done with standard biopsy punches, ports, and tubing connections as commonly applied to PDMS microfluidics. A primary disadvantage relative to PDMS is the cost of the material, which typically amounts to several US dollars per device, depending on thickness and size. The major advantages of the use of MY133 for microfluidics are its low refractive index and easy manipulation via soft photolithography.

There are many possible applications of MY133 in drug discovery and single-cell analysis using fluorescence

imaging and QPM. MY133 devices offer a way to reduce distortion and artifacts by using optically matched materials when imaging cells in direct contact with complex microfluidic structures such as in cell (Di Carlo et al. 2006; Valero et al. 2005), cell cluster (Cheng et al. 2016), embryo (Chung et al. 2011b), or organism (Chung et al. 2008) microfluidic traps. The elastic property of the MY133 polymer also makes it possible to perform fluid manipulations using pressure valves. Incorporating pressure valves for more elaborate microfluidic manipulations such as pressure-induced sorting will increase the range of potential future applications for MY133 devices. Overall, MY133 presents an attractive microfluidic material alternative for biomedical applications requiring high-precision optical imaging.

References

Andersson H, van den Berg A (2003) Microfluidic devices for cellomics: a review. Sensors Actuators B Chem 92:315–325

Baret JC et al (2009) Fluorescence-activated droplet sorting (FADS): efficient microfluidic cell sorting based on enzymatic activity. Lab Chip 9:1850–1858

Bartolo D, Degre G, Nghe P, Studer V (2008) Microfluidic stickers. Lab Chip 8:274–279

Bon P, Maucort G, Wattellier B, Monneret S (2009) Quadriwave lateral shearing interferometry for quantitative phase microscopy of living cells. Opt Expr 17(15):13080–13094

Bon P, Savatier J, Merlin M, Wattelier B, Monneret S (2012) Optical detection and measurement of living cell morphometric features with single-shot quantitative phase microscopy. J Biomed Opt 17:076004

Budwig R (1994) Refractive index matching methods for liquid flow investigations. Exp Fluids 17:350–355

Byron ML, Variano EA (2013) Refractive-index-matched hydrogel materials for measuring flow-structure interactions. Exp Fluids 54:1456

Cheng Y-H, Chen Y-C, Brien R, Yoon E (2016) Scaling and automation of a high-throughput single-cell-derived tumor sphere assay chip. Lab Chip 16:3708–3717

Choi JW et al (2002) An integrated microfluidic biochemical detection system for protein analysis with magnetic bead-based sampling capabilities. Lab Chip 2:27–30

Chun J, Zangle TA, Kolarova T, Finn RS, Teitell MA, Reed J (2012) Rapidly quantifying drug sensitivity of dispersed and clumped breast cancer cells by mass profiling. Analyst 137:5495–5498

Chung K, Crane MM, Lu H (2008) Automated on-chip rapid microscopy, phenotyping and sorting of C. elegans. Nat Methods 5:637–643

Chung C-C, Cheng I-F, Lin C-C, Chang H-C (2011a) Rapid quantification of bio-particles based on image visualisation in a dielectrophoretic microfluidic chip. Microfluid Nanofluid 10:311–319

Chung K, Kim Y, Kanodia JS, Gong E, Shvartsman SY, Lu H (2011b) A microfluidic array for large-scale ordering and orientation of embryos. Nat Methods 8:171–176

Chung BG, Lee K-H, Khademhosseini A, Lee S-H (2012) Microfluidic fabrication of microengineered hydrogels and their application in tissue engineering. Lab Chip 12:45–59

Chung K et al (2013) Structural and molecular interrogation of intact biological systems. Nature 497:332–337

Crocker JC, Grier DG (1996) Methods of digital video microscopy for colloidal studies. J Colloids Interface Sci 179:298–310

Dave FF, Hae Woon C, Burr Z, Jeremy KS, Jeffery JC, Susan VO, Lee LJ (2008) Femtosecond laser micromachining of dielectric materials for biomedical applications. J Micromech Microeng 18:035020

Di Carlo D, Wu LY, Lee LP (2006) Dynamic single cell culture array. Lab Chip 6:1445–1449

Dittrich PS, Manz A (2006) Lab-on-a-chip: microfluidics in drug discovery. Nat Rev Drug Discov 5:210–218

Ghiglia DC, Pritt MD (1998) Two-dimensional phase unwrapping: theory, algorithms, and software, vol 4. Wiley, New York

Giepmans BN, Adams SR, Ellisman MH, Tsien RY (2006) The fluorescent toolbox for assessing protein location and function. Science 312:217–224

Golden AP, Tien J (2007) Fabrication of microfluidic hydrogels using molded gelatin as a sacrificial element. Lab Chip 7:720–725

Goldstein RM, Zebker HA, Werner CL (1988) Satellite radar interferometry: two-dimensional phase unwrapping. Radio Sci 23:713–720

Groh W, Zimmermann A (1991) What is the lowest refractive index of an organic polymer? Macromolecules 24:6660–6663

Heckele M, Schomburg WK (2004) Review on micro molding of thermoplastic polymers. J Micromech Microeng 14:R1–R14

Huang S-H, Huang K-S, Liou Y-M (2016) Simultaneous monitoring of oxygen consumption and acidification rates of a single zebrafish embryo during embryonic development within a microfluidic device. Microfluid Nanofluid 21:3

Jang J, Bae CY, Park J, Ye JC (2010) Self-reference quantitative phase microscopy for microfluidic devices. Opt Lett 35:514–516

Jovic A, Howell B, Takayama S (2009) Timing is everything: using fluidics to understand the role of temporal dynamics in cellular systems. Microfluid Nanofluid 6:717–729

Kandel ME, Teng KW, Selvin PR, Popescu G (2017) Label-free imaging of single microtubule dynamics using spatial light interference microscopy. ACS Nano 11:647–655

Kim DNH, Teitell MA, Reed J, Zangle TA (2015) Hybrid random walk-linear discriminant analysis method for unwrapping quantitative phase microscopy images of biological samples. J Biomed Opt 20:111211

Kirby BJ, Hasselbrink EF (2004) Zeta potential of microfluidic substrates: 1. Theory, experimental techniques, and effects on separations. Electrophoresis 25:187–202

Lam P, Wynne KJ, Wnek GE (2002) Surface-tension-confined microfluidics. Langmuir 18:948–951

Leonard DW, Meek KM (1997) Refractive indices of the collagen fibrils and extrafibrillar material of the corneal stroma. Biophys J 72:1382–1387

Lue N, Popescu G (2006) Live cell refractometry using microfluidic devices. Opt Lett 31:2759–2761

Mazzoccoli JP, Feke DL, Baskaran H, Pintauro PN (2010) Mechanical and cell viability properties of crosslinked low-and high-molecular weight poly (ethylene glycol) diacrylate blends. J Biomed Mater Res A 93:558–566

McDonald JC, Whitesides GM (2002) Poly(dimethylsiloxane) as a material for fabricating microfluidic devices. Acc Chem Res 35:491–499

Mir M et al (2011) Optical measurement of cycle-dependent cell growth. Proc Natl Acad Sci 108:13124–13129

Ntziachristos V (2006) Fluorescence molecular imaging. Annu Rev Biomed Eng 8:1–33

Nunes PS, Ohlsson PD, Ordeig O, Kutter JP (2010) Cyclic olefin polymers: emerging materials for lab-on-a-chip applications. Microfluid Nanofluid 9:145–161

Paguirigan A, Beebe D (2006) Gelatin based microfluidic devices for cell culture. Lab Chip 6:407–413

Pérez-Madrigal MM et al (2014) Thermoplastic polyurethane: polythiophene nanomembranes for biomedical and biotechnological applications. ACS Appl Mater Interfaces 6:9719–9732

Popescu G, Park K, Mir M, Bashir R (2014) New technologies for measuring single cell mass. Lab Chip 14:646–652

Quake SR, Scherer A (2000) From micro- to nanofabrication with soft materials. Science 290:1536–1540

Reed J et al (2011) Rapid, massively parallel single-cell drug response measurements via live cell interferometry. Biophys J 101:1025–1031

Sackmann EK, Fulton AL, Beebe DJ (2014) The present and future role of microfluidics in biomedical research. Nature 507:181–189

Schmit J, Creath K, Kujawinska M (1993) Spatial and temporal phase-measurement techniques: a comparison of major error sources in one dimension. Proc SPIE 1755:202–211

Søndergaard JN et al (2010) Differential sensitivity of melanoma cell lines with BRAFV600E mutation to the specific Raf inhibitor PLX4032. J Trans Med 8:39

Sun J, Liu W, Li Y, Gholamipour-Shirazi A, Abdulla A, Ding X (2017) An on-chip cell culturing and combinatorial drug screening system. Microfluid Nanofluid 21:125

Thorsen T, Maerkl SJ, Quake SR (2002) Microfluidic large-scale integration. Science 298:580–584

Valero A, Merino F, Wolbers F, Luttge R, Vermes I, Andersson H, van den Berg A (2005) Apoptotic cell death dynamics of HL60 cells studied using a microfluidic cell trap device. Lab Chip 5:49

Vickerman V, Blundo J, Chung S, Kamm R (2008) Design, fabrication and implementation of a novel multi-parameter control microfluidic platform for three-dimensional cell culture and real-time imaging. Lab Chip 8:1468–1477

Wabuyele MB, Ford SM, Stryjewski W, Barrow J, Soper SA (2001) Single molecule detection of double-stranded DNA in poly (methylmethacrylate) and polycarbonate microfluidic devices. Electrophoresis 22:3939–3948

Wang MM et al (2005) Microfluidic sorting of mammalian cells by optical force switching. Nat Biotechnol 23:83–87

Weibel DB, Diluzio WR, Whitesides GM (2007) Microfabrication meets microbiology. Nat Rev Microbiol 5:209–218

Whitesides GM (2006) The origins and the future of microfluidics. Nature 442:368–373

Xia Y, Whitesides GM (1998) Soft lithography. Annu Rev Mater Sci 28:153–184

Yan Z, Huang X, Yang C (2017) Rapid prototyping of single-layer microfluidic PDMS devices with abrupt depth variations under non-clean-room conditions by using laser ablation and UV-curable polymer. Microfluid Nanofluid 21:108

Yeh C-H, Lin P-W, Lin Y-C (2009) Chitosan microfiber fabrication using a microfluidic chip and its application to cell cultures. Microfluid Nanofluid 8:115

Yeo LY, Chang HC, Chan PP, Friend JR (2011) Microfluidic devices for bioapplications. Small 7:12–48

Zangle TA, Teitell MA (2014) Live-cell mass profiling: an emerging approach in quantitative biophysics. Nat Methods 11:1221–1228

Zangle TA, Mani A, Santiago JG (2009) On the propagation of concentration polarization from microchannel-nanochannel interfaces part II. Numerical and experimental study. Langmuir ACS J Surf Colloids 25:3909

Zangle TA, Burnes D, Mathis C, Witte ON, Teitell MA (2013a) Quantifying biomass changes of single CD8 + T cells during antigen specific cytotoxicity. PLoS ONE 8:e68916

Zangle TA, Chun J, Zhang J, Reed J, Teitell MA (2013b) Quantification of biomass and cell motion in human pluripotent stem cell colonies. Biophys J 105:593–601

Zare RN, Kim S (2010) Microfluidic platforms for single-cell analysis. Annu Rev Biomed Eng 12:187–201